

Communication

Targeted Assembly of Ultrathin NiO/MoS₂ Electrodes for Electrocatalytic Hydrogen Evolution in Alkaline Electrolyte

Kai Xia, Meiyu Cong, Fanfan Xu, Xin Ding * and Xiaodong Zhang *

College of Chemistry and Chemical Engineering, Qingdao University, Qingdao 266071, China; xiakaiqd@163.com (K.X.); 2017020817@qdu.edu.cn (M.C.); 2018020313@qdu.edu.cn (F.X.)

* Correspondence: dingxin@qdu.edu.cn (X.D.); zhangxd@hotmail.com (X.Z.)

Received: 9 July 2020; Accepted: 5 August 2020; Published: 7 August 2020



Abstract: The development of non-noble metal catalysts for hydrogen evolution in alkaline media is highly desirable, but remains a great challenge. Herein, synergetic ultrathin NiO/MoS₂ catalysts were prepared to improve the sluggish water dissociation step for HER in alkaline conditions. With traditional electrode assembly methods, MoS₂:NiO-3:1 exhibited the best catalytic performance; an overpotential of 158 mV was required to achieve a current density of 10 mA/cm². Further, a synergetic ultrathin NiO/MoS₂/nickel foam (NF) electrode was assembled by electrophoretic deposition (EPD) and post-processing reactions. The electrode displayed higher electrocatalytic ability and stability, and an overpotential of only 121 mV was needed to achieve a current density of 10 mA/cm². The improvement was ascribed to the better catalytic environment, rather than a larger active surface area, a higher density of exposed active sites or other factors. DFT calculations indicated that the hybrid NiO/MoS₂ heterostructured interface is advantageous for the enhanced water dissociation step and the corresponding lower kinetic energy barrier—from 1.53 to 0.81 eV.

Keywords: hydrogen evolution; electrocatalyst; synergistic; binder-free; water splitting

1. Introduction

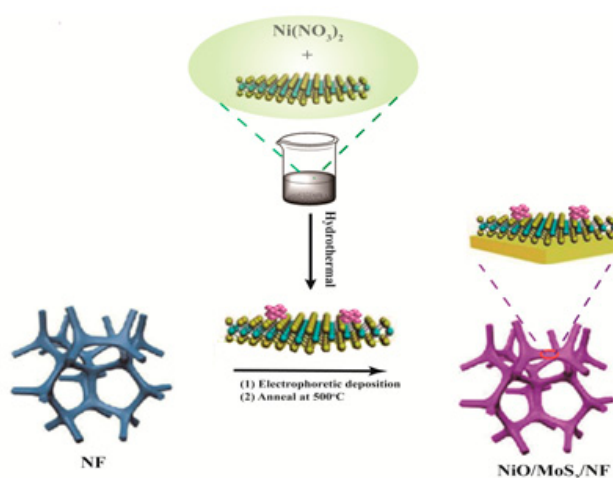
The hydrogen economy is expected to offer solutions to various problems associated with environmental pollution and fossil fuel depletion. Electrochemical water splitting to extract hydrogen is considered to be an effective way of satisfying future environmental and economic requirements for fuel sources [1–3]. High-performance and cost-effective catalysts for water splitting are a critical factor for hydrogen-based energy technologies. Generally, noble metal-based electrocatalysts such as Pt/C, Ir/C, and RuO₂ have high activities for water splitting. However, the high cost and scarcity of these elements are barriers to their applications in industrial hydrogen production. Noble metal-free electrocatalysts are commonly considered as the best choice and might address these issues [4–14]. The dissociation of water is the rate-determining reaction in aquatic hydrogen evolution and features a complex and energy intensive pathway [7,15–19], which is most effective in alkaline media [20–25]. For most metal catalysts, their hydrogen evolution reaction (HER) activity in alkaline solution is inferior compared to in acid environments, which markedly affects the development of electroactive materials [26–33]. Thus, the development of non-noble metal catalysts for the HER with a high activity for water splitting in alkaline media is of great importance.

As reported, a HER process involves water dissociation (Volmer step, $\text{H}_2\text{O} + \text{e}^- \rightarrow \text{H}_{\text{ad}} + \text{OH}^-$) and H₂ formation (Heyrovsky step, $\text{H}_2\text{O} + \text{H}_{\text{ad}} + \text{e}^- \rightarrow \text{H}_2 + \text{OH}^-$, or Tafel step, $2\text{H}_{\text{ad}} \rightarrow \text{H}_2$) in alkaline electrolytes [34,35]. The key difference between HER in acidic and alkaline media is that in an alkaline electrolyte, the kinetics are often limited by the sluggish water dissociation step.

Increasing the rate of water dissociation is currently a central problem. Fortunately, the formation of nano-interfaces between multiple phases has been confirmed to promote the water dissociation step in electrocatalysis [34–39]. Recently, Zhao et al. fabricated ultrathin transition metal dichalcogenide (MoS_2 , WS_2)/3D metal hydroxide hybridized nanosheets to enhance HER in alkaline electrolytes [35]. Jiang et al. reported mutually beneficial Co_3O_4 @ MoS_2 heterostructures, which balanced HER and OER performance by improving the kinetics of both reactions [38]. Sabbaraman et al. reported an enhanced HER activity in alkaline solution by modifying Li^+ - $\text{Ni}(\text{OH})_2$ -Pt interfaces [39]. They also found that the edges of $\text{Ni}(\text{OH})_2$ facilitated a water dissociation process, which was further promoted through Li^+ -induced destabilization of the HO–H bond. All these works provided basic theories and criterions in synthesizing HER catalysts in alkaline electrolytes. Additionally, apart from effective catalysts, a reasonable pathway to assemble electrodes with low ohmic loss and a large active surface area was also very important and urgent. In a traditional system, catalysts are assembled on the conductive substrate with Nafion [6,40–43]. This binding agent is acidic and weakly conductive, which affects the catalytic activities of the electrocatalysts by reducing conductivity and blocking active sites. However, few studies have focused on the assembly of synergetic electrodes for HER in alkaline media.

2. Materials and Methods

Herein, we introduce a simple method of assembling NiO/MoS_2 electrocatalysts with a facile method. As shown in Scheme 1 and Scheme S1, the NiO/MoS_2 composite catalysts were synthesized with different Ni contents with delaminated MoS_2 (Figure S1) [molar ratios of MoS_2 : $\text{Ni}(\text{NO}_3)_2 \cdot 6\text{H}_2\text{O}$], denoted as MoS_2 , MoS_2 : NiO -1:1, MoS_2 : NiO -2:1, MoS_2 : NiO -3:1, and MoS_2 : NiO -4:1, corresponding to the amount of added $\text{Ni}(\text{NO}_3)_2 \cdot 6\text{H}_2\text{O}$. Among these composite catalysts, MoS_2 : NiO -3:1 exhibited the best catalytic HER performance—an overpotential of 158 mV was required to achieve a current density of $10 \text{ mA}/\text{cm}^2$ in a traditional Nafion- $\text{NiO}/\text{MoS}_2/\text{GC}$ electrode construction. Furthermore, a $\text{NiO}/\text{MoS}_2/\text{NF}$ electrode was assembled by electrophoretic deposition (EPD) and post-processing reactions. (Figure S2) This electrode showed a higher electrocatalytic ability and stability than that of the Nafion-based construction and a low overpotential of 121 mV was required to achieve a current density of $10 \text{ mA}/\text{cm}^2$. This higher performance was ascribed to the optimized catalytic environment and faster HER kinetics, rather than a greater active surface area, a higher density of exposed active sites, or other factors. Hence, we established an effective pathway for assembling multi-component electrodes for HER under alkaline conditions. The results and simple synthesis method offer a promising approach to assembling multi-component electrodes for energy storage and conversion devices.



Scheme 1. Schematic of the synthesis of a synergetic NiO/MoS_2 electrode.

3. Results

The X-ray diffraction (XRD) was used to analyze the crystalline structure of the catalyst, as shown in Figure 1. Diffraction peaks at 37.2° , 43.2° , 62.8° , and 75.4° were indexed to the (111), (200), (220), and (311) planes of NiO, respectively (JCPDS No.65-5745). The diffraction peaks at 14.4° , 32.7° , 39.5° , 49.8° , 58.3° , 60.4° , 70.4° , and 72.8° are assigned to the (002), (100), (103), (105), (110), (112), (202), and (203) planes of MoS₂, respectively (JCPDS No.65-0160). Thus, we identified all characteristic peaks of MoS₂ in the XRD patterns of MoS₂:NiO-3:1. Signals from NiO were barely discernible from the baseline, owing to its low content in the composite catalyst. The NiO loading was only 1%, as measured by EDS (Figure S3). We used X-ray photoelectron spectroscopy (XPS) to investigate the components and chemical states of the NiO/MoS₂ hybrid (Figure 2). For the ultrathin MoS₂, the Mo 3*d* spectrum consisted of peaks at 229.4 and 232.6 eV, corresponding to the Mo⁴⁺ 3*d*_{5/2} and Mo⁴⁺ 3*d*_{3/2} components of MoS₂ (Figure 2A and Figure S4). In the S 2*p* spectrum, we identified doublet peaks of the 2H phase of MoS₂, S 2*p*_{1/2}, and S 2*p*_{3/2} at 163.4 and 162.2 eV, respectively (Figure 2B and Figure S5). We noted a 0.2 eV negative shift in the binding energy of Mo⁴⁺ in the results of MoS₂ and MoS₂:NiO-1:1. Furthermore, there was a small positive shift in the binding energy of the S 2*p* spectrum after formation of the NiO/MoS₂ catalyst. Ni species were in a Ni (II) state with Ni 2*p*_{1/2}, and Ni 2*p*_{3/2} signals at 856.3 and 873.7 eV, and satellite peaks at 862.5 and 880.6 eV in the XPS spectra of Ni 2*p* (Figure 2C and Figure S6). At higher NiO contents, i.e., MoS₂:NiO-4:1, there was a small positive shift in the binding energy. The maximum measured difference of 0.2 eV suggested limited charge transfer between NiO and MoS₂ [35].

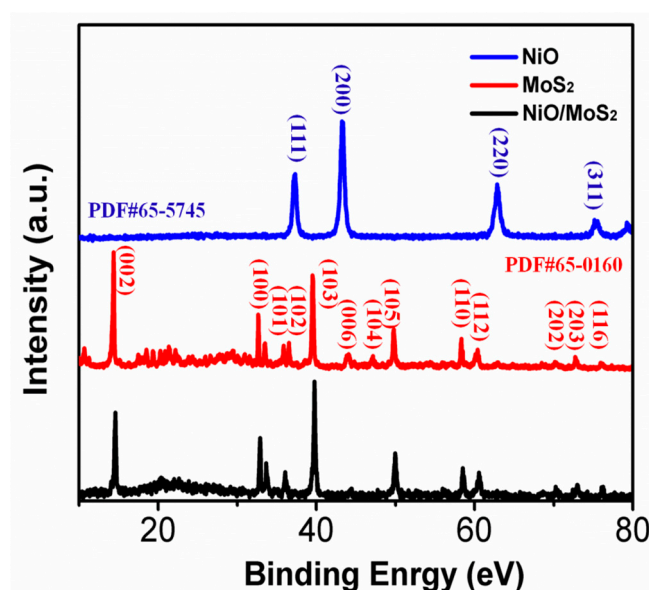


Figure 1. XRD patterns for MoS₂:NiO-3:1, NiO and MoS₂.

The morphologies and structures of the ultrathin MoS₂:NiO-3:1 were imaged with a transmission electron microscope (TEM) and atomic force microscope (AFM). The high-resolution (HR) TEM images of MoS₂:NiO-3:1 indicated the formation of NiO nanoparticles, as outlined in blue, which were tightly anchored to the MoS₂ nanosheets and uniformly dispersed. HRTEM images of the MoS₂: NiO-3:1 nanosheets showed well-resolved lattice fringes, with an interplane spacing of 0.24 nm corresponding to the (111) plane of NiO and 0.27 nm corresponding to the (100) plane of MoS₂. The HRTEM images (Figure 3A and Figure S7) and AFM (Figure 3B and Figure S8) suggested that the thickness of the monolithic laminated construction was less than 5 nm and consisted of five MoS₂ layers. Elemental mapping images also indicated a homogeneous distribution of Ni and O, as shown in Figure 3C. From XRD, XPS, HRTEM and AFM, we confirmed that NiO was prepared on ultrathin MoS₂, forming

a NiO/MoS₂ catalyst. From our TEM and AFM imaging, we further confirmed the formation of a synergetic NiO/MoS₂ catalyst.

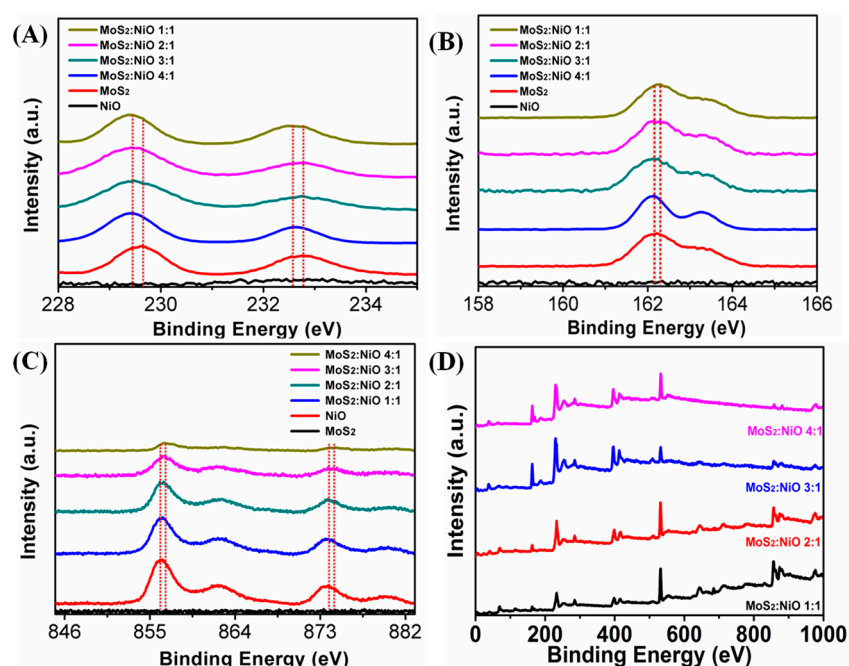


Figure 2. XPS spectra of MoS₂:NiO catalysts (D) in the Mo 3d (A), S 2p (B) and Ni 2p (C) spectral regions.

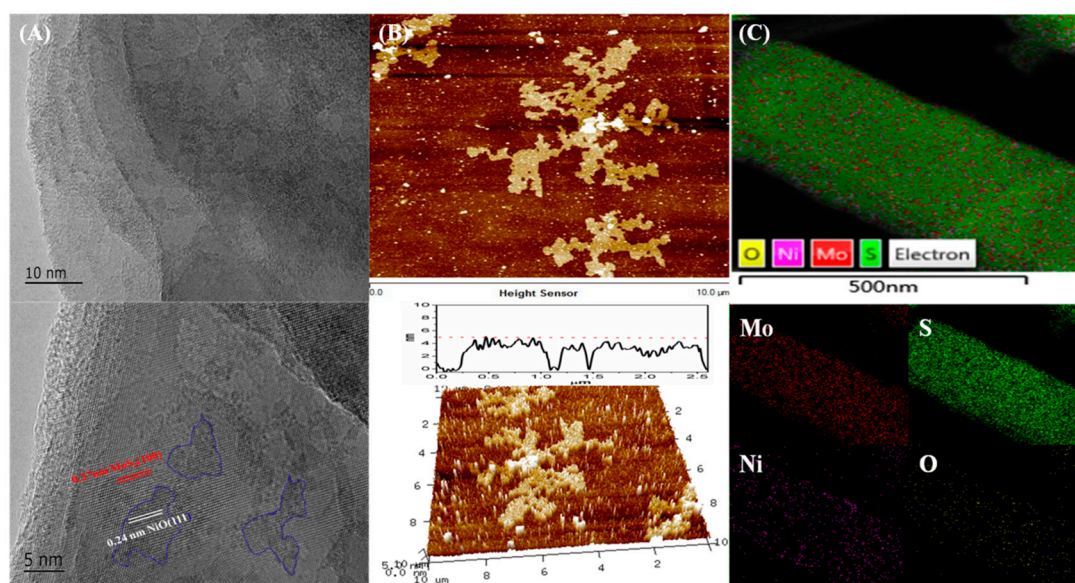


Figure 3. (A) HRTEM image of MoS₂:NiO-3:1; (B) AFM of MoS₂:NiO-3:1; (C) elemental mapping of MoS₂:NiO-3:1, showing a clear uniform distribution of Mo (red), S (green), Ni (purple), and O (yellow). Scale bars are all 500 nm.

The electrocatalytic performance was performed in a standard three-electrode system at a scan rate of 5 mV/s in a 1.0 M KOH alkaline aqueous solution. First, the electrodes were assembled in a traditional system, and the catalyst was assembled on a glass carbon electrode (GC) with Nafion. The Nafion-NiO/MoS₂/GC electrodes acted as a working electrode, and carbon rods and a Ag/AgCl electrode as the counter electrode and reference electrode, respectively. Owing to the influence of ohmic resistance, the as-measured reaction currents do not directly reflect the inherent performance of

the catalysts, therefore we applied iR compensation to all raw data, and all potentials were recorded on a reversible hydrogen electrode (RHE) scale in this work. From the linear sweep voltammetry (LSV) curves (Figure 4A), we found that the Pt/C has excellent HER activity and only required an overpotential of 109 mV to achieve a current density of 10 mA cm^{-2} . This performance ranks second only to that of electrode of Pt/C. The $\text{MoS}_2\text{:NiO-3:1}$ electrocatalyst had the lowest overpotential (η) of approximately 158 mV among that of MoS_2 (228 mV), $\text{MoS}_2\text{:NiO-1:1}$ (457 mV), $\text{MoS}_2\text{:NiO-2:1}$ (290 mV), and $\text{MoS}_2\text{:NiO-4:1}$ (213 mV). As plotted in Figure 4B, the Tafel slope of $\text{MoS}_2\text{:NiO-3:1}$ was 109 mV/dec, which was lower than that of other catalysts [MoS_2 (133 mV/dec), $\text{MoS}_2\text{:NiO-1:1}$ (161 mV/dec), $\text{MoS}_2\text{:NiO-2:1}$ (207 mV/dec), and $\text{MoS}_2\text{:NiO-4:1}$ (125 mV/dec)]. This result suggests that the HER activity can be tuned by changing the NiO content. The decrease in the Tafel slope indicates that the HER kinetics were improved by growth of NiO on ultrathin MoS_2 . Figure 4C and Figures S9–S13 show the corresponding capacitive current at 0.165 V as a function of the scan rate, which gives a double-layer capacitance (C_{dl}) of 9.4 mF/cm^2 for $\text{MoS}_2\text{:NiO-3:1}$, which is greater than that of the MoS_2 (3.2 mF/cm^2), $\text{MoS}_2\text{:NiO-1:1}$ (0.58 mF/cm^2), $\text{MoS}_2\text{:NiO-2:1}$ (0.89 mF/cm^2), and $\text{MoS}_2\text{:NiO-4:1}$ (7.5 mF/cm^2) electrode systems. Thus, a greater active surface area is one reason for the higher catalytic activity of the $\text{MoS}_2\text{:NiO-3:1}$ electrode system. We used electrochemical impedance spectroscopy (EIS) to investigate the HER kinetics of these catalysts. The Nyquist plots were fitted with the equivalent circuit inset in Figure 4D and Figure S14. The plots were fitted by a model with two parallel constant phase elements: one high frequency component related to surface porosity (R) and a low frequency component related to R_{ct} [44,45]. The value of R_{ct} was assigned as the charge transfer resistance at the interface between the catalyst and electrolyte, which is generally used to represent the electrochemical activity of an electrode. At an overpotential of 300 mV, the R_{ct} value of $\text{MoS}_2\text{:NiO-3:1}$ was much lower than that of all other catalysts. Hence, ultrathin MoS_2 modified with a moderate amount of NiO greatly reduced the charge-transfer resistance, which accelerated the HER kinetics.

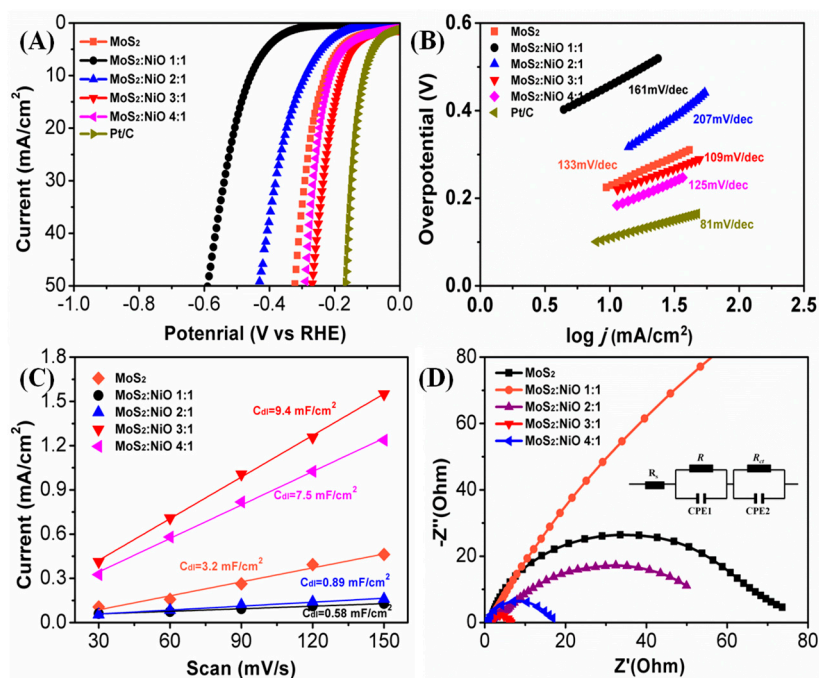


Figure 4. HER electrocatalytic activity of NiO/ MoS_2 catalysts: (A) polarization curves after iR compensation; (B) Tafel plots of electrodes at a scan rate of 5 mV/s ; (C) capacitive current at 0.165 V as a function of the scan rate; (D) EIS curves of electrodes at an overpotential of 200 mV .

We focused our attention on the most active catalyst system, $\text{MoS}_2\text{:NiO-3:1}$, and compared the results of the Nafion-NiO/ $\text{MoS}_2\text{/GC}$ and binder-free NiO/ $\text{MoS}_2\text{/NF}$ systems from the LSV curves in the electrocatalytic hydrogen evolution reaction at a scan rate of 5 mV/s . The catalyst loading

of the binder-free NiO/MoS₂/NF was controlled through the assembly time over a EPD period at a steady current density of 5 mA/cm². The quantity of Mo was accurately measured by inductively coupled plasma atomic emission spectrometry (ICP-AES), as shown in Table S1. After 5 min of EPD, the NiO/MoS₂/NF had the best performance (Figures S15 and S16, Table S1), with a low catalyst loading of 0.072 mg/cm², which was lower than that of the Nafion-NiO/MoS₂/GC system (0.106 mg/cm²). As shown in Figure 5A, an overpotential of 121 mV was required to achieve a current density of 10 mA/cm² for the binder-free NiO/MoS₂/NF, which was lower than that of NiO/MoS₂/GC (158 mV). Thus, our synthesis method yielded high-performance electrodes for HER. To confirm the enhanced HER activity of NiO/MoS₂/NF, a low Tafel slope of 99 mV/dec was measured together with a smaller C_{dl} value of 5.7 mF/cm² at a low catalyst loading (Figure S17), superior than most reported electrodes (Table S2). Thus, improved HER kinetics were the main factor contributing to the performance of this binder-free NiO/MoS₂/NF, which had a smaller active surface area and a lower density of exposed active sites compared with those features of the Nafion-based catalyst. Additionally, as shown in Figure 5D, Nyquist plots showed a considerably lower charge transfer resistance for NiO/MoS₂/NF, owing to opening of pathways with greatly reduced charge-transfer resistance in the absence of the weakly conductive Nafion membrane. Hence, the higher electrocatalytic activities of NiO/MoS₂/NF were confirmed to arise from accelerated HER kinetics and reduced charge-transfer resistance in the optimized catalytic environment rather than a larger active surface area, a higher density of exposed active sites or other factors.

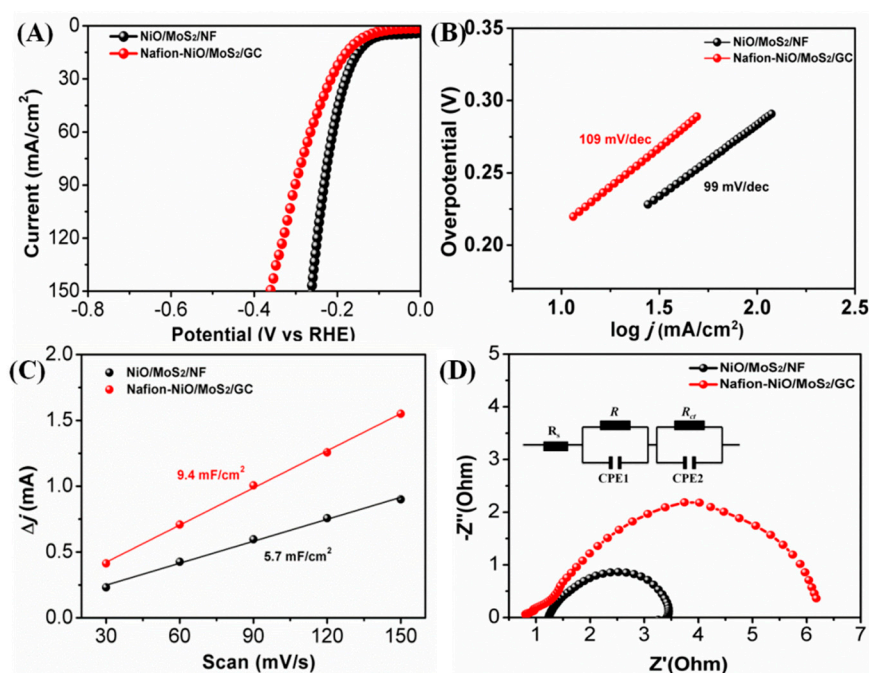


Figure 5. Electrochemical performance for HER. (A) J–V curves of representative assembling conditions: NiO/MoS₂/NF and Nafion-NiO/MoS₂/GC; (B) Tafel plots for Nafion-NiO/MoS₂/GC and NiO/MoS₂/NF; (C) capacitive current at 0.165 V as a function of the scan rate; (D) EIS curves of electrodes at an overpotential of 200 mV.

We also performed density functional theory (DFT) calculations to reveal the contributions of the hybrid NiO/MoS₂ heterostructured interface to the enhanced HER performance. Because the basal plane of MoS₂ is catalytically inert to HER, we focused on the Mo edge. Optimized structures of MoS₂ with a zigzag edge (i.e., a Mo edge saturated with S) and the hybrid MoS₂/NiO (111) are shown in Figure S18, and the corresponding reaction pathways for H₂O dissociation over MoS₂ and the MoS₂/NiO (111) hybrid are presented in Figure 6. At the MoS₂/NiO (111) interface, strong chemical bonding between S and the surface under coordinated Ni was observed, which resulted in severe

reconstruction of the Ni (111) surface. From Figure 6, we note that H₂O adsorption at the MoS₂ edge is very weak (an adsorption energy of -0.06 eV). Moreover, the dissociation of H₂O into adsorbed H and OH over the MoS₂ edge is energetically endothermic, requiring an input of approximately 1.21 eV, and has an extremely high energy barrier (1.53 eV) to overcome; hence, water dissociation at pure MoS₂ is thermodynamically unfavorable. However, with the assistance of NiO, the H₂O adsorption becomes stronger at surface Ni sites (-0.46 eV), and the reaction energy and the kinetic activation barrier of H₂O dissociation decrease to 0.48 and 0.81 eV, respectively. In the dissociated state, H is bound to the S edge, whereas OH is bonded to the surface Ni. Thus, both the thermodynamics and kinetics of the water dissociation step (i.e., the rate-determining step of HER under alkaline conditions) can be effectively promoted by hybridization of MoS₂ with NiO, which is in good agreement with our experimental observations.

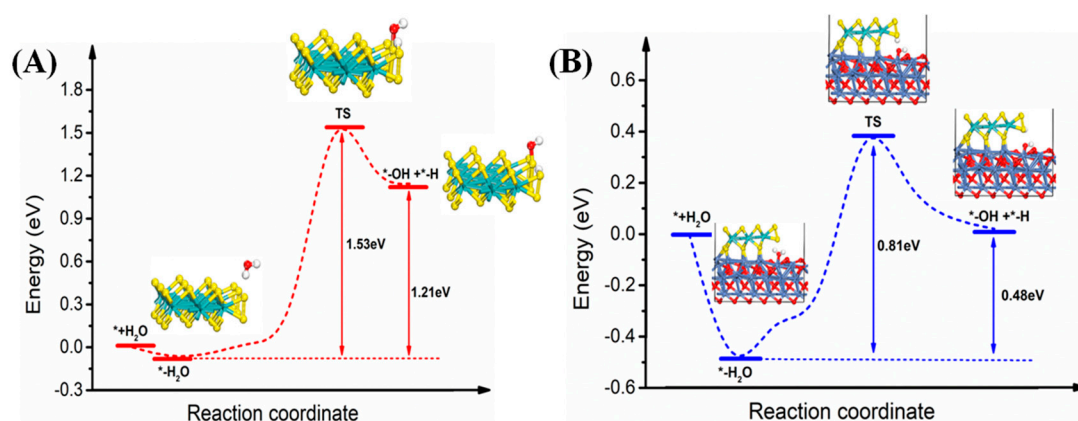


Figure 6. Energy pathway for water dissociation at the MoS₂ zigzag edge (A) and the MoS₂/NiO (111) interface (B) with atomic configurations of initial state (water adsorption), transition state (TS) and final state (water dissociation). The reaction energy and the activation barrier are indicated in the inset.

4. Conclusions

In conclusion, ultrathin NiO/MoS₂ catalysts were prepared to promote the water dissociation step for HER in alkaline conditions. The combined experimental measurements and DFT calculations suggest that the hybrid NiO/MoS₂ heterostructured interface was responsible for the enhanced water dissociation step and corresponding lower kinetic energy barrier. With the use of traditional electrode assembly methods, the MoS₂:NiO-3:1 catalyst exhibited the best catalytic HER performance, and an overpotential of 158 mV was required to achieve a current density of 10 mA/cm². Furthermore, a binder-free NiO/MoS₂/NF electrode was also assembled by EPD and post-processing reactions. This electrode had better electrocatalytic performance and stability, with an overpotential of only 121 mV required to achieve current density of 10 mA/cm², which is clearly superior to the performance of the traditional electrodes. We attribute these improvements to the better catalytic environment and faster HER kinetics. Thus, we have introduced an effective pathway for assembling synergetic multi-component electrodes for HER under alkaline conditions for the first time. These results and the simple synthesis method offer a promising direction for assembling synergetic multi-component electrodes for energy storage and conversion devices.

Supplementary Materials: The following are available online at <http://www.mdpi.com/2079-4991/10/8/1547/s1>, Scheme S1: Schematic of the synthesis of synergetic NiO/MoS₂ electrode, Figure S1: (A) The SEM image of pure MoS₂. (B) SEM of the MoS₂ after exfoliation, Figure S2: (A, B) Different resolution SEM images of NiO/MoS₂/NF electrode, Figure S3: The EDX mapping for NiO/MoS₂ catalyst powder, Figure S4: XPS spectra of Mo 3d regions of NiO/MoS₂ catalysts, Figure S5: XPS spectra of S 2p regions of NiO/MoS₂ catalysts, Figure S6: XPS spectra of Ni 2p regions of NiO/MoS₂ catalysts, Figure S7: HRTEM image of MoS₂:NiO-3:1, Figure S8: AFM of MoS₂:NiO-3:1, Figure S9: CVs of MoS₂:NiO 3:1 (A) and corresponding Cdl (B), Figure S10: CVs of MoS₂:NiO 4:1 (A) and corresponding Cdl (B), Figure S11: CVs of MoS₂ (A) and corresponding Cdl (B), Figure S12: CVs of MoS₂:NiO 2:1

(A) and corresponding Cdl (B), Figure S13: CVs of MoS₂:NiO 1:1 (A) and corresponding Cdl (B), Figure S14: EIS curves of NiO/MoS₂/NF at different overpotential from 100–300 mV, Figure S15: LSV curves for NiO/MoS₂/NF under various electrophoresis time, Figure S16: LSV curves for NiO/MoS₂/NF before and after 500 CV cycle (left); Stability test of the NiO/MoS₂/NF electrode at a fixed current density of 10 mA/cm² for HER, Figure S17: CV curves for NiO/MoS₂/NF, Figure S18: Optimized structures of MoS₂ with zigzag edge (a) and the hybrid MoS₂/NiO(111) (b, side view). Color modes: yellow for S, green for Mo, red for O and cyan for Ni, Table S1: The Overpotential of different electrodes at 10 and 50 mA/cm², Table S2: A representative summary of HER performances of nonprecious materials based electrocatalysts previously reported catalyst for HER in 1M KOH aqueous solution.

Author Contributions: Conceptualization, X.D. and K.X.; M.C.; F.X.; methodology, K.X., M.C.; software, K.X.; validation, X.D.; and X.Z.; formal analysis, X.D.; investigation, X.D.; resources, X.D.; data curation, X.D.; writing—original draft preparation, X.K., M.C.; F.X.; writing—review and editing, X.D.; and X.Z.; visualization, X.D.; supervision, X.D.; project administration, X.D.; funding acquisition, X.D.; All authors have read and agreed to the published version of the manuscript.

Funding: This research was funded by the National Natural Science Foundation of China (Grant No: 21908120), the Natural Science Foundation of Shandong Province (Grant No: ZR2018BB037) and the project of Qingdao Applied Basic Research Programs of Science and Technology (Grant No: 18-2-2-10-jch and 18-2-2-35-jch).

Conflicts of Interest: The author declares that they have no conflict to interest.

References

1. Dresselhaus, M.S.; Thomas, I.L. Alternative energy technologies. *Nature* **2001**, *414*, 332–337. [[CrossRef](#)] [[PubMed](#)]
2. Yang, X.J.; Hu, H.; Tan, T.; Li, J. China's renewable energy goals by 2050. *Environ. Dev.* **2016**, *20*, 83–90. [[CrossRef](#)]
3. Li, P.; Chen, W. Recent advances in one-dimensional nanostructures for energy electrocatalysis. *Chin. J. Catal.* **2019**, *40*, 4–22. [[CrossRef](#)]
4. Zhou, J.; Dou, Y.B.; Zhou, A.; Guo, R.M.; Zhao, M.J.; Li, J.R. MOF Template-Directed Fabrication of Hierarchically Structured Electrocatalysts for Efficient Oxygen Evolution Reaction. *Adv. Energy Mater.* **2017**, *7*, 1602643. [[CrossRef](#)]
5. Hu, H.; Guan, B.; Xia, B.; Lou, X.W. Designed Formation of Co₃O₄/NiCo₂O₄ Double-Shelled Nanocages with Enhanced Pseudocapacitive and Electrocatalytic Properties. *J. Am. Chem. Soc.* **2015**, *137*, 5590–5595. [[CrossRef](#)] [[PubMed](#)]
6. Zhao, S.; Wang, Y.; Dong, J.; He, C.T.; Yin, H.; An, P.; Zhao, K.; Zhang, X.; Gao, C.; Zhang, L.; et al. Ultrathin metal–organic framework nanosheets for electrocatalytic oxygen evolution. *Nat. Energy* **2016**, *1*, 16184. [[CrossRef](#)]
7. He, P.; Yu, X.Y.; Lou, X.W. Carbon-Incorporated Nickel-Cobalt Mixed Metal Phosphide Nanoboxes with Enhanced Electrocatalytic Activity for Oxygen Evolution. *Angew. Chem. Int. Ed.* **2017**, *56*, 3897–3900. [[CrossRef](#)]
8. Yuan, C.Z.; Sun, Z.T.; Jiang, Y.F.; Yang, Z.K.; Jiang, N.; Zhao, Z.W.; Qazi, U.Y.; Zhang, W.H.; Xu, A.W. One-Step In Situ Growth of Iron-Nickel Sulfide Nanosheets on FeNi Alloy Foils: High-Performance and Self-Supported Electrodes for Water Oxidation. *Small* **2017**, *13*, 1604161. [[CrossRef](#)]
9. Wu, H.; Chen, Z.; Zhang, J.; Wu, F.; Xiao, F.; Du, S.; He, C.; Wu, Y.; Ren, Z. Generalized Synthesis of Ultrathin Cobalt-Based Nanosheets from Metallophthalocyanine-Modulated Self-Assemblies for Complementary Water Electrolysis. *Small* **2018**, *14*, 1702896. [[CrossRef](#)]
10. Wu, D.; Wei, Y.; Ren, X.; Ji, X.; Liu, Y.; Guo, X.; Liu, Z.; Asiri, A.M.; Wei, Q.; Sun, X. Co(OH)₂ Nanoparticle-Encapsulating Conductive Nanowires Array: Room-Temperature Electrochemical Preparation for High-Performance Water Oxidation Electrocatalysis. *Adv. Mater.* **2018**, *30*, 1705366. [[CrossRef](#)]
11. Wu, J.; Ge, X.B.; Li, Z.H.; Cao, D.; Xiao, J.Y. Highly dispersed NiCoP nanoparticles on carbon nanotubes modified nickel foam for efficient electrocatalytic hydrogen production. *Electrochim. Acta* **2017**, *252*, 101–108. [[CrossRef](#)]
12. Xiao, C.H.; Zhang, B.; Li, D. Partial-sacrificial-template Synthesis of Fe/Ni Phosphides on Ni Foam: A Strongly Stabilized and Efficient Catalyst for Electrochemical Water Splitting. *Electrochim. Acta* **2017**, *242*, 260–267. [[CrossRef](#)]

13. Gao, X.; Qi, J.; Wan, S.; Zhang, W.; Wang, Q.; Cao, R. Conductive Molybdenum Sulfide for Efficient Electrocatalytic Hydrogen Evolution. *Small* **2018**, *14*, e1803361. [[CrossRef](#)] [[PubMed](#)]
14. Cong, M.; Sun, D.; Zhang, L.; Ding, X. In situ assembly of metal-organic framework-derived N-doped carbon/Co/CoP catalysts on carbon paper for water splitting in alkaline electrolytes. *Chin. J. Catal.* **2020**, *41*, 242–248. [[CrossRef](#)]
15. Ding, X.; Zhang, L.L.; Wang, Y.; Liu, A.H.; Gao, Y. Design of photoanode-based dye-sensitized photoelectrochemical cells assembling with transition metal complexes for visible light-induced water splitting. *Coord. Chem. Rev.* **2018**, *357*, 130–143. [[CrossRef](#)]
16. Ding, X.; Gao, Y.; Zhang, L.L.; Yu, Z.; Liu, J.H.; Sun, L.C. Visible Light-Driven Water Splitting in Photoelectrochemical Cells with Supramolecular Catalysts on Photoanodes. *ACS Catal.* **2014**, *4*, 2347–2350. [[CrossRef](#)]
17. Gao, Y.; Ding, X.; Liu, J.; Wang, L.; Lu, Z.; Li, L.; Sun, L. Visible light driven water splitting in a molecular device with unprecedentedly high photocurrent density. *J. Am. Chem. Soc.* **2013**, *135*, 4219–4222. [[CrossRef](#)]
18. Wang, Z.; Liu, H.; Ge, R.; Ren, X.; Ren, J.; Yang, D.; Zhang, L.; Sun, X. Phosphorus-Doped Co₃O₄ Nanowire Array: A Highly Efficient Bifunctional Electrocatalyst for Overall Water Splitting. *ACS Catal.* **2018**, *8*, 2236–2241. [[CrossRef](#)]
19. Huang, T.; Shen, T.; Gong, M.; Deng, S.; Lai, C.; Liu, X.; Zhao, T.; Teng, L.; Wang, D. Ultrafine Ni-B nanoparticles for efficient hydrogen evolution reaction. *Chin. J. Catal.* **2019**, *40*, 1867–1873. [[CrossRef](#)]
20. Indra, A.; Paik, U.; Song, T. Boosting Electrochemical Water Oxidation with Metal Hydroxide Carbonate Templated Prussian Blue Analogues. *Angew. Chem. Int. Ed.* **2018**, *57*, 1241–1245. [[CrossRef](#)]
21. Zhou, D.; Cai, Z.; Lei, X.; Tian, W.; Bi, Y.; Jia, Y.; Han, N.; Gao, T.; Zhang, Q.; Kuang, Y.; et al. NiCoFe-Layered Double Hydroxides/N-Doped Graphene Oxide Array Colloid Composite as an Efficient Bifunctional Catalyst for Oxygen Electrocatalytic Reactions. *Adv. Energy Mater.* **2018**, *8*, 1701905. [[CrossRef](#)]
22. Gu, Y.; Chen, S.; Ren, J.; Jia, Y.A.; Chen, C.; Komarneni, S.; Yang, D.; Yao, X. Electronic Structure Tuning in Ni₃FeN/r-GO Aerogel toward Bifunctional Electrocatalyst for Overall Water Splitting. *ACS Nano* **2018**, *12*, 245–253. [[CrossRef](#)] [[PubMed](#)]
23. Zhang, F.S.; Wang, J.W.; Luo, J.; Liu, R.R.; Zhang, Z.M.; He, C.T.; Lu, T.B. Extraction of nickel from NiFe-LDH into Ni₂P@NiFe hydroxide as a bifunctional electrocatalyst for efficient overall water splitting. *Chem. Sci.* **2018**, *9*, 1375–1384. [[CrossRef](#)] [[PubMed](#)]
24. Fan, K.; Chen, H.; Ji, Y.; Huang, H.; Claesson, P.M.; Daniel, Q.; Philippe, B.; Rensmo, H.; Li, F.; Luo, Y.; et al. Nickel-vanadium monolayer double hydroxide for efficient electrochemical water oxidation. *Nat. Commun.* **2016**, *7*, 11981. [[CrossRef](#)] [[PubMed](#)]
25. Sun, X. Ni foam-supported NiCoP nanosheets as bifunctional electrocatalysts for efficient overall water splitting. *Chin. J. Catal.* **2019**, *40*, 1405–1407. [[CrossRef](#)]
26. Tian, J.; Liu, Q.; Asiri, A.M.; Sun, X. Self-supported nanoporous cobalt phosphide nanowire arrays: An efficient 3D hydrogen-evolving cathode over the wide range of pH 0–14. *J. Am. Chem. Soc.* **2014**, *136*, 7587–7590. [[CrossRef](#)]
27. Shi, H.; Liang, H.; Ming, F.; Wang, Z. Efficient Overall Water-Splitting Electrocatalysis Using Lepidocrocite VOOH Hollow Nanospheres. *Angew. Chem. Int. Ed. Engl.* **2017**, *56*, 573–577. [[CrossRef](#)]
28. Xue, Z.H.; Su, H.; Yu, Q.Y.; Zhang, B.; Wang, H.H.; Li, X.H.; Chen, J.S. Janus Co/CoP Nanoparticles as Efficient Mott-Schottky Electrocatalysts for Overall Water Splitting in Wide pH Range. *Adv. Energy Mater.* **2017**, *7*, 1602355. [[CrossRef](#)]
29. Wu, Z.X.; Wang, J.; Zhu, J.; Guo, J.P.; Xiao, W.P.; Xuan, C.J.; Lei, W.; Wang, D.L. Highly efficient and stable MoP-RGO nanoparticles as electrocatalysts for hydrogen evolution. *Electrochim. Acta* **2017**, *232*, 254–261. [[CrossRef](#)]
30. Gupta, S.; Patel, N.; Fernandes, R.; Hanchate, S.; Miotello, A.; Kothari, D.C. Co-Mo-B Nanoparticles as a non-precious and efficient Bifunctional Electrocatalyst for Hydrogen and Oxygen Evolution. *Electrochim. Acta* **2017**, *232*, 64–71. [[CrossRef](#)]
31. Liu, Y.R.; Hu, W.H.; Han, G.Q.; Dong, B.; Li, X.; Shang, X.; Chai, Y.M.; Liu, Y.Q.; Liu, C.G. Novel CoP Hollow Prisms as Bifunctional Electrocatalysts for Hydrogen Evolution Reaction in Acid media and Overall Water-splitting in Basic media. *Electrochim. Acta* **2016**, *220*, 98–106. [[CrossRef](#)]
32. Lei, H.; Chen, M.; Liang, Z.; Liu, C.; Zhang, W.; Cao, R. Ni₂P hollow microspheres for electrocatalytic oxygen evolution and reduction reactions. *Catal. Sci. Technol.* **2018**, *8*, 2289–2293. [[CrossRef](#)]

33. Chen, M.; Qi, J.; Zhang, W.; Cao, R. Electrosynthesis of NiP_x nanospheres for electrocatalytic hydrogen evolution from a neutral aqueous solution. *Chem Commun.* **2017**, *53*, 5507–5510. [[CrossRef](#)]
34. Wang, Y.; Kong, B.; Zhao, D.Y.; Wang, H.T.; Selomulya, C. Strategies for developing transition metal phosphides as heterogeneous electrocatalysts for water splitting. *Nano Today* **2017**, *15*, 26–55. [[CrossRef](#)]
35. Zhu, Z.; Yin, H.; He, C.T.; Mamun, M.A.; Liu, P.; Jiang, L.; Zhao, Y.; Wang, Y.; Yang, H.G.; Tang, Z.; et al. Ultrathin Transition Metal Dichalcogenide/3d Metal Hydroxide Hybridized Nanosheets to Enhance Hydrogen Evolution Activity. *Adv Mater.* **2018**, *30*, e1801171. [[CrossRef](#)]
36. Shang, B.; Ma, P.; Fan, J.; Jiao, L.; Liu, Z.; Zhang, Z.; Chen, N.; Cheng, Z.; Cui, X.; Zheng, W. Stabilized monolayer 1T MoS₂ embedded in CoOOH for highly efficient overall water splitting. *Nanoscale* **2018**, *10*, 12330–12336. [[CrossRef](#)] [[PubMed](#)]
37. Liu, J.; Zheng, Y.; Zhu, D.; Vasileff, A.; Ling, T.; Qiao, S.Z. Identification of pH-dependent synergy on Ru/MoS₂ interface: A comparison of alkaline and acidic hydrogen evolution. *Nanoscale* **2017**, *9*, 16616–16621. [[CrossRef](#)]
38. Liu, J.; Wang, J.; Zhang, B.; Ruan, Y.; Wan, H.; Ji, X.; Xu, K.; Zha, D.; Miao, L.; Jiang, J. Mutually beneficial Co₃O₄@MoS₂ heterostructures as a highly efficient bifunctional catalyst for electrochemical overall water splitting. *J. Mater. Chem. A.* **2018**, *6*, 2067–2072. [[CrossRef](#)]
39. Subbaraman, R.; Tripkovic, D.; Strmcnik, D.; Chang, K.C.; Uchimura, M.; Paulikas, A.P.; Stamenkovic, V.; Markovic, N.M. Enhancing hydrogen evolution activity in water splitting by tailoring Li(+)-Ni(OH)(2)-Pt interfaces. *Science* **2011**, *334*, 1256–1260. [[CrossRef](#)]
40. Ma, Y.Y.; Wu, C.X.; Feng, X.J.; Tan, H.Q.; Yan, L.K.; Liu, Y.; Kang, Z.H.; Wang, E.B.; Li, Y.G. Highly efficient hydrogen evolution from seawater by a low-cost and stable CoMoP@C electrocatalyst superior to Pt/C. *Energy Environ. Sci.* **2017**, *10*, 788–798. [[CrossRef](#)]
41. Ye, L.; Chai, G.L.; Wen, Z.H. Zn-MOF-74 Derived N-Doped Mesoporous Carbon as pH-Universal Electrocatalyst for Oxygen Reduction Reaction. *Adv. Funct. Mater.* **2017**, *27*, 1606190. [[CrossRef](#)]
42. Tabassum, H.; Guo, W.H.; Meng, W.; Mahmood, A.; Zhao, R.; Wang, Q.F.; Zou, R.Q. Metal-Organic Frameworks Derived Cobalt Phosphide Architecture Encapsulated into B/N Co-Doped Graphene Nanotubes for All pH Value Electrochemical Hydrogen Evolution. *Adv. Energy Mater.* **2017**, *7*, 1601671. [[CrossRef](#)]
43. Yang, F.; Zhao, P.; Hua, X.; Luo, W.; Cheng, G.; Xing, W.; Chen, S. A cobalt-based hybrid electrocatalyst derived from a carbon nanotube inserted metal-organic framework for efficient water-splitting. *J. Mater. Chem. A.* **2016**, *4*, 16057–16063. [[CrossRef](#)]
44. Lin, H.; Zhang, W.; Shi, Z.; Che, M.; Yu, X.; Tang, Y.; Gao, Q. Electrospinning Hetero-Nanofibers of Fe₃C-Mo₂C/Nitrogen-Doped-Carbon as Efficient Electrocatalysts for Hydrogen Evolution. *ChemSusChem* **2017**, *10*, 2597–2604. [[CrossRef](#)] [[PubMed](#)]
45. Zhang, Y.Q.; Xia, X.H.; Cao, X.; Zhang, B.W.; Tjep, N.H.; He, H.Y.; Chen, S.; Huang, Y.Z.; Fan, H.J. Ultrafine Metal Nanoparticles/N-Doped Porous Carbon Hybrids Coated on Carbon Fibers as Flexible and Binder-Free Water Splitting Catalysts. *Adv. Energy Mater.* **2017**, *7*, 1700220. [[CrossRef](#)]

